Remote Sens. **2015**, *7*, 836-864; doi:10.3390/rs70100836

OPEN ACCESS

remote sensing

ISSN 2072-4292

www.mdpi.com/journal/remotesensing

Article

Use of Radarsat-2 and Landsat TM Images for Spatial Parameterization of Manning's Roughness Coefficient in Hydraulic Modeling

Joseph Mtamba [1,2,*], Rogier van der Velde [2], Preksedis Ndomba [1], Vekerdy Zoltán [2,3] and Felix Mtalo [1]

1 Department of Water Resources Engineering, University of Dar es Salaam, P.O. Box 35131, 14115 Dar es Salaam, Tanzania; E-Mails: pmndomba@udsm.ac.tz (P.N); mtalo@wrep.udsm.ac.tz (F.M.)

2 Department of Water Resources, Faculty of Geo-Information and Earth Observation (ITC), University of Twente, P.O. Box 6, AA Enschede7500, The Netherlands; E-Mails: r.vandervelde@utwente.nl (R.V.); z.vekerdy@utwente.nl (Z.V.)

3 Department of Water and Waste Management, Szent István University, Gödöllő, 2100 Páter Károly utca 1., Hungary

***** Author to whom correspondence should be addressed; E-Mail: joseph.mtamba@udsm.ac.tz; Tel.: +254-784-635-977; Fax: +255-222-410-029.

Academic Editor: Nicolas Baghdadi and Prasad S. Thenkabail

Received: 21 March 2014 / Accepted: 23 December 2014 / Published: 14 January 2015

Abstract: Vegetation resistance influences water flow in floodplains. Characterization of vegetation for hydraulic modeling includes the description of the spatial variability of vegetation type, height and density. In this research, we explored the use of dual polarized Radarsat-2 wide swath mode backscatter coefficients (σ°) and Landsat 5 TM to derive spatial hydraulic roughness. The spatial roughness parameterization included four steps: (i) land use classification from Landsat 5 TM; (ii) establishing a relationship between σ° statistics and vegetation parameters; (iii) relative surface roughness (K_s) determination from Synthetic Aperture Radar (SAR) backscatter temporal variability; (iv) derivation of the spatial distribution of the spatial hydraulic roughness both from Manning's roughness coefficient look up table (LUT) and relative surface roughness. Hydraulic simulations were performed using the FLO-2D hydrodynamic model to evaluate model performance under three different hydraulic modeling simulations results with different Manning's coefficient parameterizations, which includes SWL1, SWL2 and SWL3. SWL1 is simulated water

levels with optimum floodplain roughness (n_p) with channel roughness n_c = 0.03 $m^{-1/3}$/s; SWL2 is simulated water levels with calibrated values for both floodplain roughness n_p = 0.65 $m^{-1/3}$/s and channel roughness n_c = 0.021 $m^{-1/3}$/s; and SWL3 is simulated water levels with calibrated channel roughness n_c and spatial Manning's coefficients as derived with aid of relative surface roughness. The model performance was evaluated using Nash-Sutcliffe model efficiency coefficient (E) and coefficient of determination (R^2), based on water levels measured at a gauging station in the wetland. The overall performance of scenario SWL1 was characterized with E = 0.75 and R^2 = 0.95, which was improved in SWL2 to E = 0.95 and R^2 = 0.99. When spatially distributed Manning values derived from SAR relative surface values were parameterized in the model, the model also performed well and yielding E = 0.97 and R^2 = 0.98. Improved model performance using spatial roughness shows that spatial roughness parameterization can support flood modeling and provide better flood wave simulation over the inundated riparian areas equally as calibrated models.

Keywords: synthetic aperture radar; hydraulic roughness; relative surface roughness; vegetation mapping; hydraulic modeling

1. Introduction

Riparian wetland ecosystems are flooded on multiple occasions every year, as floods are generated from excess rainfall in the catchment. The alteration of hydraulic regime in the river affects several ecological processes in the wetland floodplains, e.g., ecosystem productivity, species distribution and occurrence, nutrients and sediment dynamics [1–4]. To predict the impacts of flood wave on the floodplain, the hydraulic processes of the river have to be assessed at optimal temporal and spatial scales using hydraulic models. Several efforts have been made to develop hydraulic models that can simulate flow patterns and predict extreme flood levels in rivers and floodplains [5–10]. The development of an accurate and reliable hydraulic model that well describes surface water flow across a large wetland floodplain depends on topographic data and hydraulic roughness, *viz*. Manning's roughness of the floodplain [11,12]. Manning's roughness is one of the key variables of a hydraulic model; vegetation component plays a crucial role in the total resulting roughness, especially in vegetated floodplains. High hydraulic roughness values reduce wave celerity and rise flood depth [13,14]. The uncertainty of roughness parameterization leads to errors in water level estimation and affects the hydrograph characteristics.

The hydraulic roughness of a floodplain depends on factors, such as the type and structure of vegetation, the cross section area, obstructions in the channel and floodplain as well as the degree of meandering [15,16]. Different approaches have been used to quantify the hydraulic roughness across floodplains, e.g., using tabulated reference roughness coefficients, visually inspecting and comparing photographs of floodplain reaches and assigning the appropriate roughness values to similar floodplains [16] and using a momentum balance to define the hydraulic impacts of vegetation [11,17,18]. On small floodplain areas conventional ground surveys have been used [19]. Systematic detection, identification and assessment of riparian vegetation using conventional field sampling are often unachievable as these techniques are time-consuming and expensive.

Remote sensing techniques, e.g., vegetation mapping, terrestrial laser scanning and digital parallel photography, have been proven useful in determination of vegetation types, density and height [19–23]. Different techniques of remote sensing of hydraulic roughness have been discussed in detail by Forzieri *et al.* [24]. These techniques include classification-derived hydraulic maps and estimation of vegetation hydrodynamic properties. The vegetation maps are obtained from classification of digital satellite images, and a hydraulic roughness value is assigned to each vegetation type then, based on a look-up table (LUT). This approach does not provide spatial variability of hydraulic roughness within a vegetation class. The second method of estimating hydraulic roughness is based on *in-situ* defined biomechanical properties of vegetation, e.g., height, density, but this requires extended complementary ground surveys that can be feasible only at local scale [19,23]. The benefits of calibrating of hydraulic model using this approach are to support determination of spatial hydraulic indices more accurately for other studies that requires calibrated hydraulic model, e.g., sedimentation deposition assessment.

Previous studies in riparian environments using spectral remote sensing data have focused on classifying vegetation [25–30]. The applied LUTs were based on literature (e.g., [8,15,16]). Despite some encouraging results, the problem of the lack of within-class variability of the roughness coefficients was obvious, since differences in vegetation height and density within the class should have yielded different Manning's roughness values [31]. In fact, different arboreal patterns, bushes and meadows, can have similar spectral signatures and cannot be always differentiated in optical satellite imagery. There is, therefore, a need to define new approaches that can support characterizing the spatial variability of the hydraulic roughness for large floodplains based on vegetation biophysical characteristics.

Synthetic Aperture Radar (SAR) is a remote sensing technique that enables the construction of high-resolution images from active microwave observations. In essence, these active microwave instruments quantify the apparent roughness of the target surface that is largely defined by the geometry and to lesser extent by the moisture content of the surface. As such, SAR observations have been used in the past for soil moisture monitoring [32,33], flood mapping [34–36] and vegetation mapping [37–43]. The SAR backscatter is controlled by vegetation structure, surface geometry and dielectric properties of the ground targets [44]. The dielectric properties are influenced by soil moisture and vegetation water content [32,44]. Microwave radiation penetrates vegetation canopies interacting with the canopy scatterers, *i.e.*, leaves, twigs, branches, and the trunk [45]. Cross-polarization ratio can be used to determine relative surface roughness (K_s) variations within the vegetation class, identifying different areas with varying vegetation densities and types. Estimation of vegetation structure depends on multi-polarization scattering of SAR signals. Mattia *et al.* [46] studied the effect of surface roughness on multi frequency polarimetric L and C band data and found that depolarization ratio can be used to discriminate different types of vegetation canopies especially forest and non-forest areas. The depolarization ratio is equivalent to cross-polarization ratio in other literature. The cross-polarization ratio is characterized by surface and volume scattering mechanism at the vegetation canopy surface, while co-polarization ratio is characterized by surface and volume scattering (including tree trunk and branches mechanism). A study on vegetation canopy cover by Mathiew *et al.* [22] on savannah woody vegetation using C-band Quad- Polarization Fine Beam RADARSAT-2 imagery found that dry period HV polarization can be effectively used to predict structural metrics. The added advantage of the use of SAR in this research is to derive relative surface roughness that is correlated to biophysical properties of vegetation to support spatial variability of the hydraulic roughness within vegetation types.

The main objective of this paper is to investigate the possible advantage of spatially distributed hydraulic roughness parameterization for hydraulic modeling of floodplains in comparison to a single hydraulic roughness value for the whole floodplain and a set of hydraulic roughness values defined per vegetation type.

2. Material

2.1. Study Area

The Mara wetland (Figure 1) is one of the largest tropical wetland systems in East Africa, which has drawn attention for conservation. To understand hydrology and hydrodynamic processes in the wetland floodplain reliable models need to be developed. Mara wetland receives most of its water from the Mara River, originating from the Mau escarpment forest, passing through vast low-lying plains including the transboundary Masai Mara/Serengeti national parks, and releasing water into Lake Victoria. Floods typically occur during the months of November/December and April/May with water depths varying from 0.5 to 2 m in the floodplain. The riverbeds of the main Mara River and its tributaries are fairly well defined at their upper reaches, but become increasingly meandering as they approach the confluence with the Tigithe River. The decreasing slope reduces the downstream river velocity and increases deposition, a characteristic for most fluvial systems.

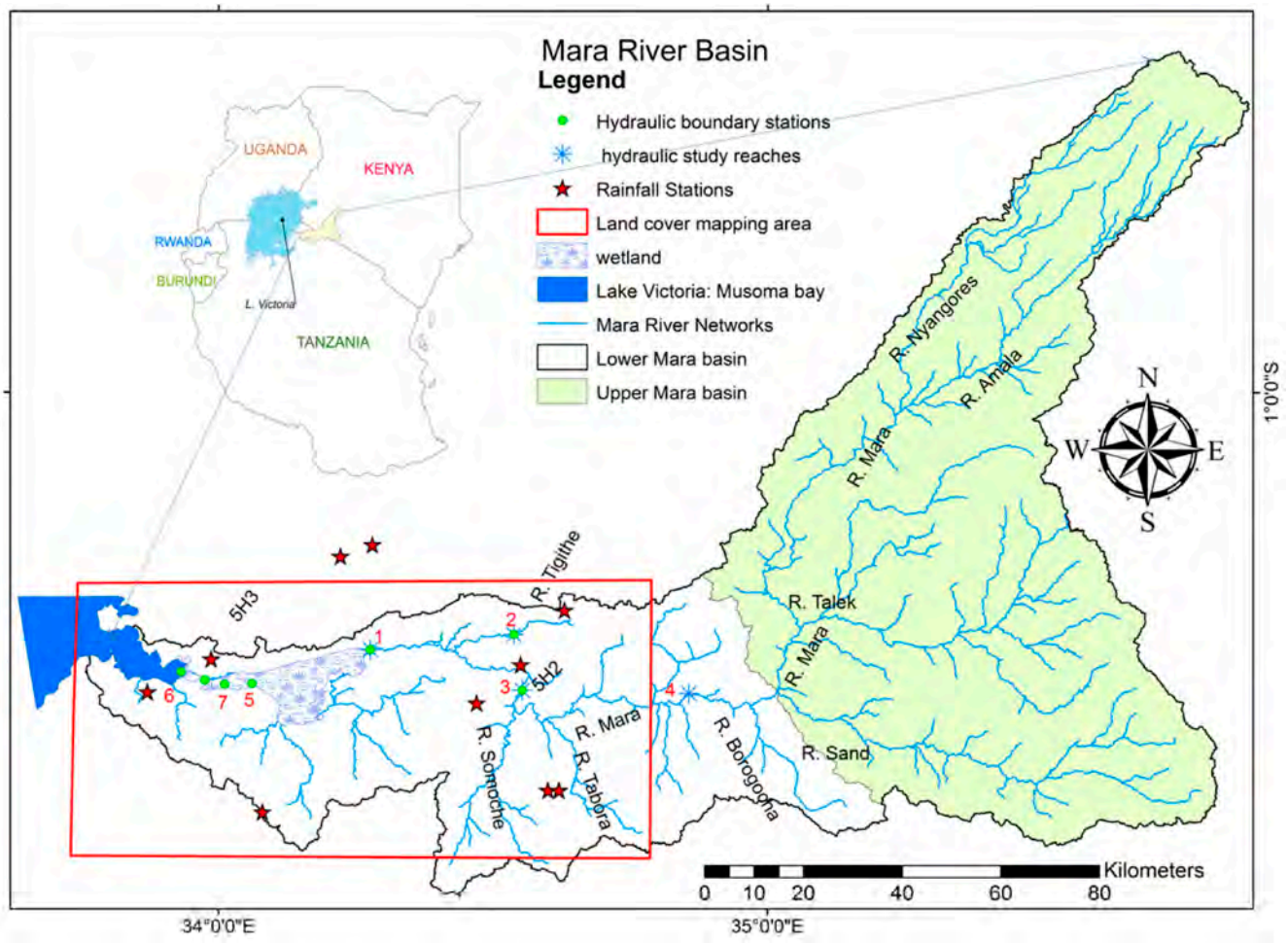

Figure 1. Location of the study area (rectangle) within the lower Mara River basin.

The Lower Mara Basin has ten rain-gauging stations and five river water level measuring stations at Bisarwi (1), Tigithe bridge (2), Mara mine (5H2) (3), Kogatende (4) and Kirumi ferry (5H3). The development of rating curves for stations (1)–(4) is described in Mtamba *et al.* [47]. The Mara mines and Kirumi ferry gauging stations have been in operation since 1969. The other stations were specifically installed to support the flood modeling and understanding reach-scale hydraulics in 2011–2013 [47,48]. The figure below shows historical gauging stations and temporary stations for hydraulic study (1–4). Mara mine (5H2) falls in both categories.

2.2. Field Measurements and Remote Sensing Data

2.2.1. Rainfall and River Discharge Measurements

Rainfall data was obtained from the Lake Victoria Basin Office at Musoma office. The rainfall gauging stations are equipped with standard rain gauges. The measurement accuracy is about 0.5 mm. The rainfall data from ten gauging stations in the lower Mara Basin were analyzed and averaged using Thiessen polygon approach to obtain daily rainfall in mm/day.

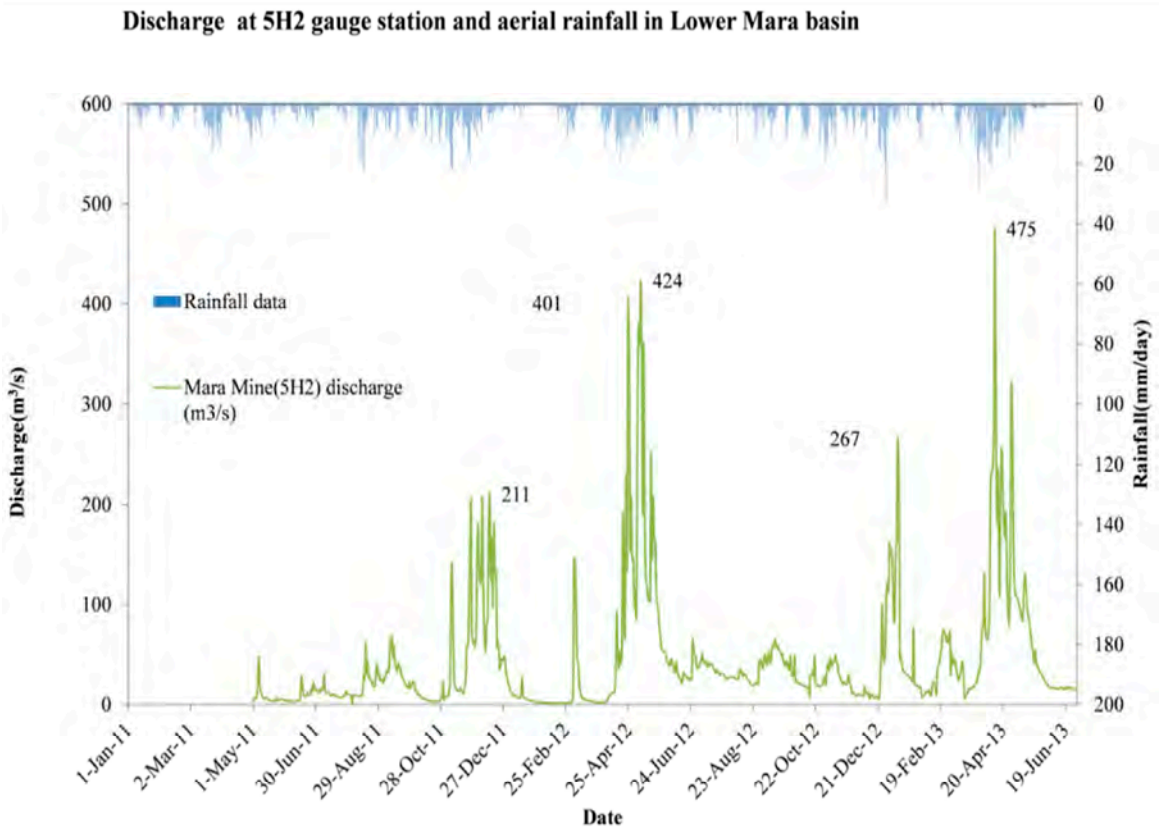

Figure 2. Discharge and areal rainfall at Mara mine gauging station. The values show four flood events during November/December and April/May.

The gauging stations in the study area were equipped with staff gauges. Mara Mine and Tigithe bridge gauging station is located upstream of the wetland floodplain. The stations are equipped with standard gauge staff plates of 1m for water level measurements in the river. The measurements are taken manually twice a day at 9:00 and 15:00 h. The daily levels records are averaged to obtain average daily values.

These water levels are converted to river discharge using a calibrated rating curve [47]. The two-year flow hydrograph for Mara Mine (Figure 2) highlights two distinct flood periods, namely in November/December and April/May. During these events a maximum discharge of 475 $m^3 \cdot s^{-1}$ was recorded. The floods are generated by surface runoff in response to convective rain events of several mm per day across the Mara River Basin.

2.2.2. Vegetation Characterization

A detailed vegetation survey was done in October 2010 and September 2013. During the 2010 field campaign, the vegetation data collected in each site included type of vegetation/land use (e.g., grassland, dense green papyrus and shrub/thicket). It was not possible to undertake the collection of the wetland ground reference data concurrently with the acquisition dates of the images. However, information from locals suggests that there were no significant changes on land cover between the image acquisition and the fieldwork dates. It was considered that the wetland floodplain grassland changes significantly between wet season and dry season due to rainfall and grazing by herds of cattle. The main objective of the 2010 field visit was to collect data to support wetland vegetation classification for the study area. 300 ground truth points were recorded and classified in the field (Table 1). Figure 3 provides sample photos of vegetation in the area.

Table 1. Field vegetation classification in 2010.

S/No	Land Cover Class	Land Cover Characteristics
1	Water	Open water: Water without plant cover (in rivers, lagoons, oxbow lakes, ponds *etc.*)
2	Swamps	Swamps: Sediment deposited areas, burned papyrus vegetation, sediment laden waters
3	Partially submerged vegetation	Sparse green vegetation: vegetation which include papyrus, grassland with water background or partially submerged
4	Papyrus/thicket	Dense green vegetation: Dark green vegetation which includes green papyrus, trees, bushes
5	Regenerated papyrus/shrub	Very sparse green vegetation: Regenerated vegetation which include papyrus, grassland with water background or partially submerged
6	Eichorrhoea crassipes/grassland	Grassland: Eichoria crassipes vegetation, lush grassland,
7	Agriculture/bare land	Bare land: open Bare land, settlement, houses, open farms, dry grass, clouds
		Total

During the 2013 field visit, the objective was to collect independent data sets for vegetation attributes to derive Plant Area Index (PAI) for the herbaceous pattern vegetation (papyrus and reeds) and Fractional Vegetation Cover (FVC) for the arboreal and shrub classes (shrub/thicket and floodplain forest).

2.2.3. Landsat 5 TM Imagery and Preprocessing

Landsat Thematic Mapper (TM) is a multispectral scanning radiometer that was carried onboard Landsat 4 and 5. The TM sensors have provided nearly continuous data in the period of

1 March 1984–05 June 2013. TM data was collected in seven bands, which cover the visible, near-infrared, shortwave, and thermal infrared spectral bands of the electromagnetic spectrum. All bands have a resolution of 30 m except the thermal band that has a resolution of 120 m, with a swath width of 185 km. The thermal band was excluded during the present analysis due to its coarser spatial resolution and the different physical processes involved in the observation. Landsat provides data acquisition over the Earth's landmass with a repeat cycle of 16 days.

Figure 3. Photos showing different land cover types in the area.

From 2009 to 2013, there are several Landsat images present in USGS Global Visualization Viewer (GLOVIS) database (http://glovis.usgs.gov). Preliminary observation was used to select cloud free images during non-flooded seasons. Normalized Difference Vegetation Index (NDVI) for each image was determined and used to select images that can be used to describe vegetation classes in the study area. The Landsat TM acquired on 11 June 2009 was selected for vegetation mapping in the Lower Mara Basin. The image was atmospherically corrected using the ATCOR module in the ERDAS Imagine software and geometrically transformed with tie points onto a topographic map of the area. A subset of the area was extracted for the further analysis.

2.2.4. Radarsat 2 Imagery and Preprocessing

The RADARSAT-2 satellite was launched on 14 December 2007 by the Canadian Space Agency (CSA). It is carrying a SAR sensor operating at a center frequency of 5.405 GHz (C-band). The system is capable of acquiring backscatter observations (σ°) in various imaging modes including single (HH or VV) polarization; dual co- and cross-polarization combinations (HH/HV, VV/VH) with several image swaths. The imagery used for the present study is comprised of a series of 12 VV/VH polarized RADARSAT-2 wide swath mode images from April 2011 to August 2012. The SAR images were received as preprocessed level-1 SAR Georefferenced Fine Product (1SGF) with 25 m × 28 m resolution for a 150 km × 150 km area covering a view angle range of 20–45 degrees.

The Next ESA SAR Toolbox (NEST) was utilized to process the Radarsat-2 data sets to calibrated backscatter (σ°) products through application of the Range Doppler terrain correction utility. A median filter with a 5 × 5 kernel size was applied to the σ° data sets to suppress the speckle noise inherent to the SAR data. After filtering, the images were reprojected to UTM zone 36 WGS84 coordinate system subsetted for the area of interest and automatically co registered.

3. Methods

3.1. Overall Framework

Developing large-scale hydraulic models requires appropriate data to describe flow resistance in the model domain. There is a need to investigate how friction component can be parameterized to improve model performance hence to minimize the efforts for calibration and validation of hydraulic models. The approach used in this study includes derivation of Manning's coefficients derived from the spectral and radar images by combining Manning's LUT and relative surface roughness. Landsat imagery was used to derive vegetation classes to which minimum and maximum Manning's roughness coefficients were assigned from literature. The SAR imagery was used to determine K_s from cross-polarization ratio. The spatial distribution of the hydraulic roughness values was then determined from combining K_s maps and Manning's LUT values. The roughness was averaged per vegetation class to obtain mean roughness values per vegetation class. A FLO-2D hydraulic model was set up to check the improvement of model performance when different scenarios of roughness parameterization were implemented. The overall framework is summarized in Figure 4 below.

3.2. PAI and FVC Retrieval

The PAI and FVC are ratios describing the fraction of area covered by vegetation per unit area of ground surface. The higher the PAI or the FVC the higher the vegetation density is, hence the higher is the hydraulic roughness. PAI was determined from 35 sites for herbaceous vegetation using the gap fraction approach. In papyrus and reed vegetation, four to five vertical photographs were taken below the canopy at each site; an approach of determining the vegetation gap fraction. This method is based on simplified models of light transmission into the canopy. A variety of approaches for estimating PAI using direct and indirect methods were presented by Bréda [49], Jonckheere *et al.* [50] and Weiss *et al.* [51]. Vegetation gap fraction (G) is defined as the fraction of sky seen from below the canopy [49–52]. Gap

fraction is related to PAI ($PAI = 1 - G$). Images were processed using a segmentation algorithm implemented in the ILWIS software. The segmentation process was developed to classify open sky pixels and cloudy sky pixels according to their chromatic values. The segmentation process is simply based on the pixels intensity assuming that vegetation elements appear darker than the sky. Figure 5a shows a sample image of vertical photographs was taken below the vegetation canopy. Figure 5b shows the results of image after segmentation process, dark areas are areas covered by vegetation and white areas are clasified as open sky. Areal average PAI was calculated for each sampled location. FVC was determined for 10 plots of 100 m × 100 m in the arboreal and shrub land cover classes. The crown base diameters of each vegetation type were measured with measuring tape at each plot. The FVC was calculated as the fraction of total surface area covered by arboreal and shrub vegetation. Results are summarized in Table 2.

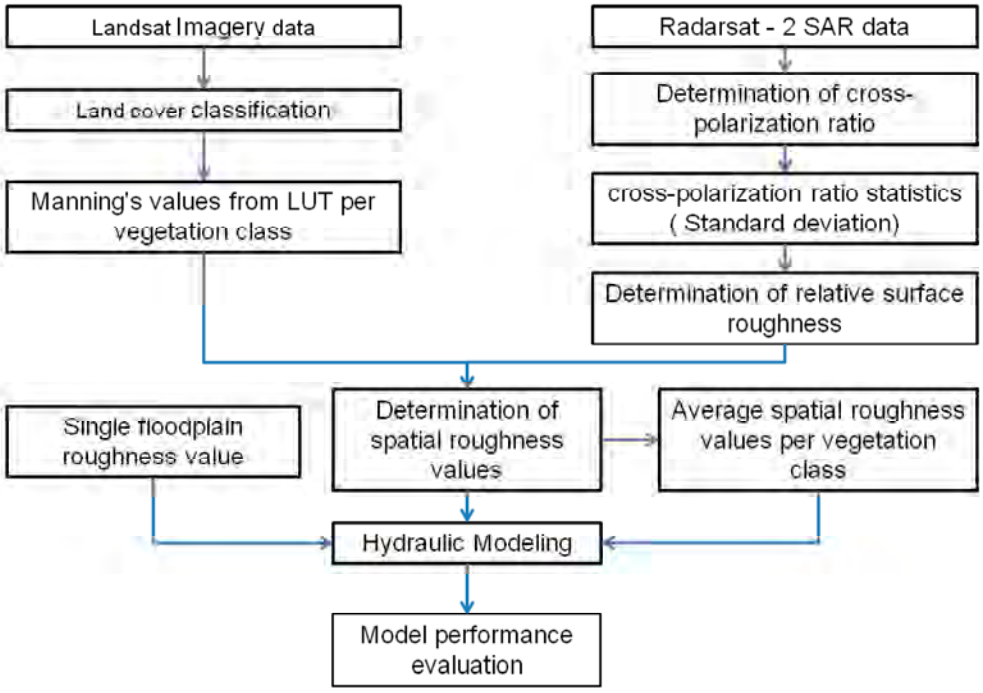

Figure 4. Overall framework of research approach.

Figure 5. Canopy photos at a reed site (**a**) Vertical photo taken below the canopy (**b**) image after segmentation.

Table 2. Plant Area Index (PAI) and Fractional Vegetation Cover (FVC) measured *in situ* at different sites.

	Vegetation Type	No of Samples	PAI (1) and FVC (2)			
			Min	Max	Mean	Standard Deviation
1	Papyrus	15	0.335	0.867	0.710	0.121
	Reeds	20	0.223	0.871	0.725	0.145
2	Shrub/Thicket	10	0.401	0.860	0.674	0.140

3.3. Vegetation Classification from Landsat TM Imagery

Supervised classification was done to determine vegetation types in the study area. Visual interpretation of the Landsat TM true color composite bands (321) and combination of NDVI was used to assist in the collection of the training set for classification. Training sites for each vegetation class were identified and a classification scheme prepared for classification process. Maximum likelihood classification was done using the ERDAS Imagine 2013 software, resulting in 7 vegetation classes. The result was cleaned by applying a median filter of 5 × 5 pixels to remove isolated pixels. The accuracy assessment was done as recommended by Congalton and Green [53], using 300 data points from the field survey, which were not used in the training process.

3.4. Vegetation Class Characterization Based on Backscatter Statistics

3.4.1. SAR Images

It is well understood that the backscatter (σ°) is affected by the dielectric properties of the scattered surface or volume (in our case the wetland) and the scattering geometry. Due to the large difference between the dielectric constants of water and the other materials, the backscatter is determined by the water content in as well as on the vegetation and the soil, furthermore, the vegetation morphology and the land surface roughness. To investigate the vegetation dynamics in the study area and period visually, an RGB color composite for Vertically transmitted and Vertically received signals (VV polarization) and Vertically transmitted and Horizontally received signals (VH polarization) (Green—VH polarization; Red and Blue—VV polarization) was made each of the available twelve images in total (Figure 6a–l). It can be observed that within the wetland, the greenish colors represent small differences between VV and VH backscatter signals, which indicate the presence of vegetation [22]. The reddish color highlights large VV *versus* VH backscatter, associated with bare land. The black areas refer to low VV and VH backscatter, related to smooth surfaces, usually open water bodies and flooded areas. In order to avoid the bare lands and the effect of temporary flooding on the backscatter of vegetated areas, five SAR scenes with high level of reddish and black coloration on floodplain were excluded from the further analysis. Rainfall and river discharge data has been used also to confirm flooded situations in the image selection.

From the visual interpretation of these SAR images, backscatter variations in densely vegetated, deep-rooted areas are more stable than in less dense areas (e.g., grass) during different seasons. In densely vegetated areas the backscatter response is more or less constant during all seasons because in the floodplain, they can maintain their water content even during the dry season. Floods and rainfall

events are also a major cause of high backscatter variation in flood plains as can be seen in the images acquired on the dates of 12 March 2011 and 18 May 2012.

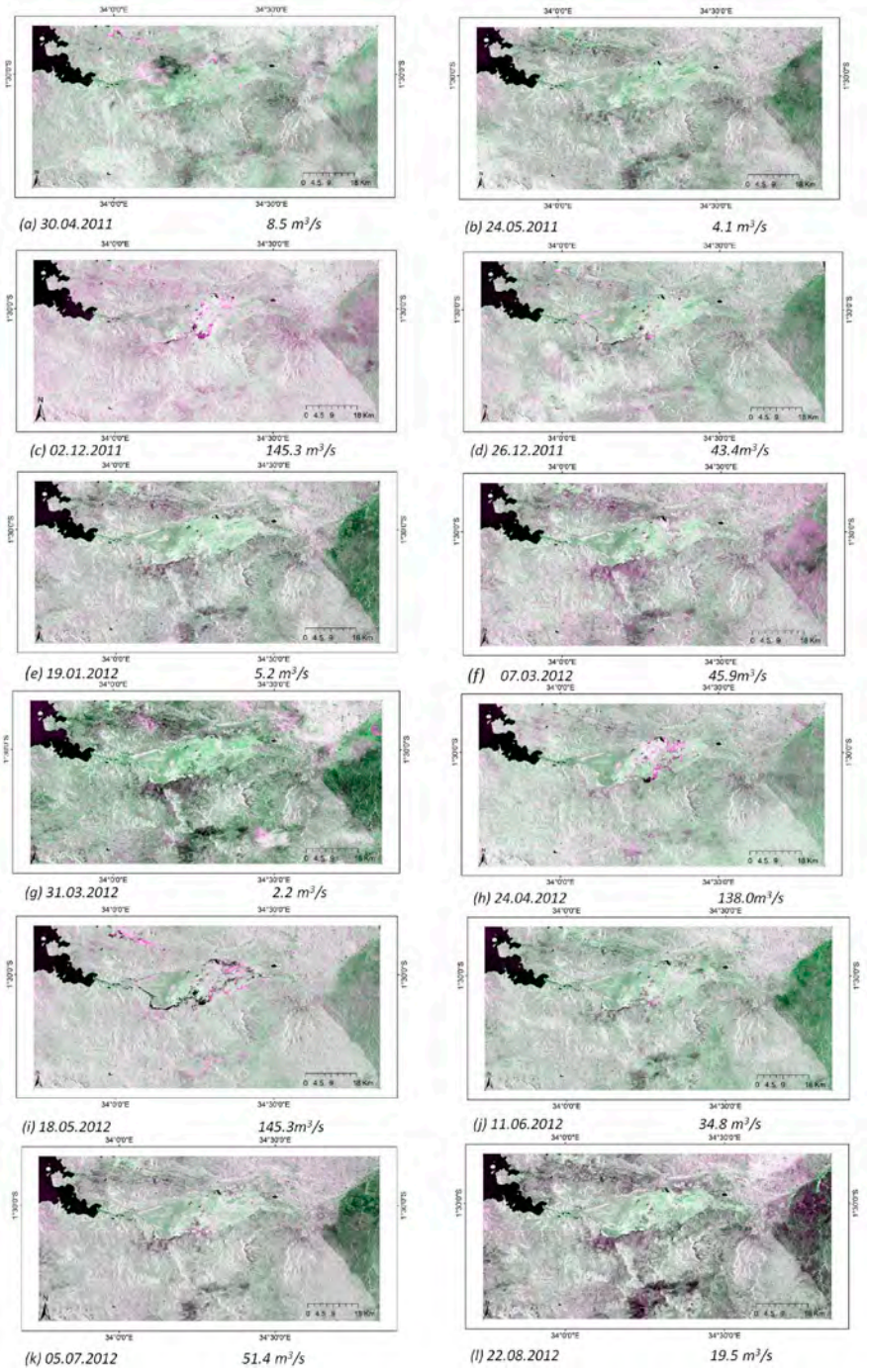

Figure 6. Sub figures **a**–**l** above shows RGB color composite images for 12 Radarsat-2 SAR images acquired over the Lower Mara Basin. Image aquisation dates and average daily river discharge values are shown in the bottom of each image. RGB color composite imageries are attributting to VV, VH and VV polarization for Red, Green and Blue channels respectively.

Figure 6a–l shows RGB color composite for 12 SAR imagery used in this study and river discharge data for the Mara Mine gauging station. These data were used to aid selection of images for the subsequent analysis of vegetation attributes. Initial temporal variability assessment was done on all

images and it was observed that vegetated areas affected by flood cannot be separated clearly from grassland areas. Therefore uniformity of rainfall and flood spread within the images was used as the key criteria of selection of images. The minimum number of images for multitemporal analysis was also limited as recommended by Maghsoudi *et al.*, (2011) [54]. From Figure 6, SAR scenes of 2 December 2011, 7 March 2012, 24 April 2012, 18 May 2012 and 22 August 2012 were excluded from the vegetation analysis because of the influence of floods and rainfall that caused high temporal variability of the backscatter.

3.4.2. Backscatter Characterization and Statistics

The estimators of temporal variability of multitemporal SAR data sets include standard deviation, normalized standard deviation, saturation, maximum-minimum ratio of σ° in dB [55]. In this study, we used mean, maximum and standard deviation of the seven selected SAR images. The mean VV and VH polarization does not provide clear separation between vegetation classes. In Figure 7a,b, the standard deviation identifies the flooded vegetation formations and monitor non-flooded vegetation phenology. The Figure 7a,b for standard deviation maps of VV and VH polarized σ° respectively shows a separation between densely vegetated areas (papyrus, floodplain forest) and other less vegetated areas. Standard deviation of σ° measures the variability encountered in the polarimetric SAR images. In the agricultural fields, the temporal variability is high because of the influence of soil moisture changes, vegetation phenology and growth, cultivation practice (e.g. grazing).

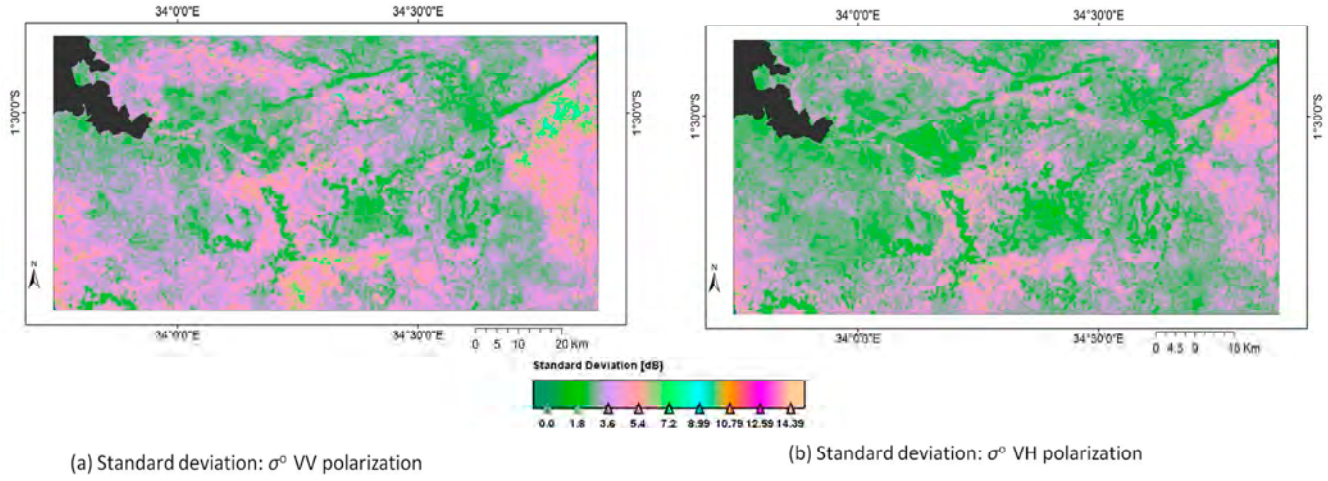

Figure 7. Standard deviation of the backscatter (in dB) for (**a**) Vertically transmitted and Vertically received signals (VV polarization) and (**b**) Vertically transmitted and Horizontally received signals (VH polarization) on the study area characterizing temporal variability of the backscatter. Areas with higher vegetation have low standard deviation than areas with shorter vegetation e.g., grasslands.

High mean σ° and low standard deviation was observed in aquatic vegetation and forest/thicket/papyrus vegetation areas. In floodplain grassland and less dense vegetation intermediate σ° and high standard deviation were observed. Agricultural/grassland areas outside the floodplain are characterized by low σ° and high standard deviation. Figure 7 shows the temporal variability statistic (standard deviation) for the analyzed SAR imagery.

Figure 8 shows temporal variation of backscatter statistic on vegetation types in some specific selected sites. It can be observed that standard deviation provides a clearer separation between vegetation types than the mean backscatter values.

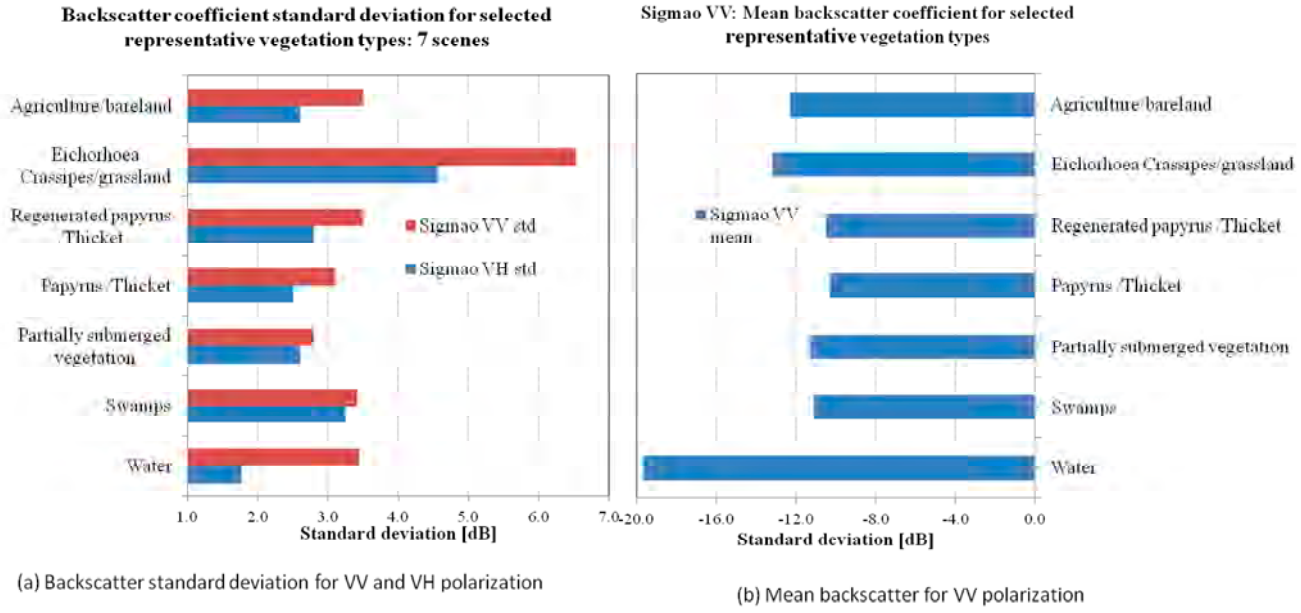

Figure 8. Backscatter statistics for different vegetation types for (**a**) Standard deviation (std) for VV and VH polarization (**b**) Mean for VV polarization. Sigmao represents σ°. Sigmao VV std is standard deviation of VV polarisation; Sigmao VV mean is average of VV polarisation and Sigmao VH std is standard deviation of VH polarization for the selected seven images.

3.5. Determination of the Spatial Distribution of the Hydraulic Roughness

3.5.1. Concept

Hydraulic vegetation roughness refers to the resistance force exerted by vegetation on water flowing over or through it [23]. Rough vegetation reduces water flow velocity and leads to higher water levels and thus increases flood risks. Height and density of submerged vegetation and density of emergent vegetation are the key characteristics from which roughness parameters in hydraulic models are derived. The parameter describing emergent vegetation, such as forest, is vegetation density [56]. Hydraulic vegetation density is the sum of the projected plant areas in the direction of the flow per unit volume. The parameters describing submerged vegetation, such as grassland, reed, or herbs are vegetation height and density [57]. The spatial distribution of these vegetation characteristics is an essential input for hydrodynamic models.

SAR data was investigated for quantitative assessment of floodplain relative hydraulic roughness, which is related to vegetation height and density. Grassland is hydraulically smooth, forests and dense shrubs are hydraulically rough [15]. This concept is analogous where grassland had high temporal variability of backscatter and forests have low temporal variability of VH polarized σ° which describes volume scattering mechanism ($dB \cdot m^{-3}$). In addition variability of VV polarized σ° can describe surface

scattering mechanism (dB·m^{-2}). The variability of the ratio of volume to surface backscattering can describe vegetation density differences (m^{-1}) within a vegetation type. This ratio is described by the cross-polarization ratio and its exponential inversion provides values at a scale of 0 to 1, describing smooth to rough surface within the vegetation class, further on referred to a relative surface roughness.

3.5.2. Implementation

Cross-polarization ratio of the seven SAR images and their descriptive statistical parameters were calculated. It was observed that the standard deviation of the cross-polarization ratio can be used to determine relative surface roughness variations within the vegetation class. The inversion was based on the exponential Markov Random Fields (MRF) model. The MRF is a global model uniquely determined by a local statistical description of a single image or multispectral images for image pattern analysis, texture modeling and image classification [58–64]. In this paper, we use MRF model to determine relative surface roughness from standard deviation of cross-polarized ratio of series of SAR imagery. The empirical inversion technique used for series of cross-polarization ratio images based on Equation (1). The equation assumes that the relative roughness parameters follow the Markovian probability density function (pdf). Equation (1) was used to determine the relative surface roughness map of the study area.

$$\boldsymbol{K_s} = \frac{\mathbf{1}}{\mathbf{Z}} \boldsymbol{e}^{-\boldsymbol{\rho_{std}}} \tag{1}$$

$$\boldsymbol{\rho_{std}} = \sqrt{\frac{\mathbf{1}}{\boldsymbol{N}} \sum_{\boldsymbol{i=1}}^{\boldsymbol{N}} (\boldsymbol{\rho_i} - \boldsymbol{\mu})^2} \tag{2}$$

$$\boldsymbol{\rho_i} = \frac{\boldsymbol{\sigma^o_{VH_i}}}{\boldsymbol{\sigma^o_{VV_i}}} \tag{3}$$

where;

$\boldsymbol{K_s}$ = relative surface roughness [-]
$\boldsymbol{z}$ = correction factor [-], for this case considered to be 1 for the Markovian pdf
$\boldsymbol{\rho_{std}}$ = standard deviation of cross-polarized ratio of series of SAR imagery [dB]
$\boldsymbol{N}$ = number of SAR imagery used in analysis
$\boldsymbol{\rho_i}$ = cross-polarization ratio of SAR imagery *i*
$\boldsymbol{\mu}$ = mean of cross polarization ratio of SAR imagery used in analysis
$\boldsymbol{\sigma^o_{VH_i}}$ = VH polarization of SAR imagery *i* [dB]
$\boldsymbol{\sigma^o_{VV_i}}$ = VV polarization of SAR imagery *i* [dB]

3.5.3. Hydraulic Roughness Map

The relative roughness was used to aid the spatial parameterization of the Manning's roughness within the vegetation classes. Numerous researchers give guidance on selection of Manning's values for various vegetation classes [6,8,12,15,65]. After a careful review and investigation of Manning's values by comparing the study site vegetation characteristics and those given in the literature, the value ranges shown in Table 3 were adopted for the study area. These values should not be considered as the actual,

since their determination is based on vegetation classes and Manning's values found in the literature. Table 3 is LUT for Manning's coefficient ranges for each vegetation class.

Table 3. Manning's roughness ranges for different vegetation classes referred from Chow [15] and O'Brien [8].

		a	b	c
No	**Vegetation Class**	$n_{min,c}$ ($m^{-1/3}/s$)	$n_{ave,c}$ ($m^{-1/3}/s$)	$n_{max,c}$ ($m^{-1/3}/s$)
1	Water	0.02	0.03	0.085
2	Swamps	0.09	0.2	0.34
3	Partially submerged vegetation	0.17	0.3	0.48
4	Papyrus/ Thicket	0.17	0.3	0.8
5	Regenerated papyrus/Shrub	0.2	0.4	0.4
6	Eichorrhoea Crassipes/ Grassland	0.2	0.3	0.3
7	Agriculture/ bare soil	0.1	0.2	0.3

Spatial hydraulic roughness was calculated by Equation (4) below. This equation assumes a linear increase of Manning's coefficient with relative surface roughness within the vegetation class.

$$\boldsymbol{n_{i,c} = n_{min,c} + (n_{max,c} - n_{min,c}) \frac{(K_s)_{i,c} - (K_s)_{min,c}}{(K_s)_{max,c} - (K_s)_{min,c}}} \quad (4)$$

where;

$\boldsymbol{n_{i,c}}$ = Manning's roughness value for a cell within a vegetation class ($m^{-1//3}/s$)
$\boldsymbol{n_{min,c}}$ = minimum Manning's roughness value for a cell within a vegetation class ($m^{-1//3}/s$)
$\boldsymbol{n_{max,c}}$ = maximum Manning's roughness value for a cell within a vegetation class ($m^{-1//3}/s$)
$\boldsymbol{(K_s)_{i,c}}$ = relative surface roughness value for a cell within a vegetation class (-)
$\boldsymbol{(K_s)_{min,c}}$ = minimum relative surface roughness value for a cell within a vegetation class (-)
$\boldsymbol{(K_s)_{max,c}}$ = maximum relative surface roughness value for a cell within a vegetation class (-)

3.6. Hydraulic Modeling

The derived hydraulic parameters were used in the FLO-2D River modeling software. FLO-2D model is a two-dimensional (2D) hydrodynamic model developed by FLO-2D Software *Inc*—Arizona, USA (http://www.flo-2d.com). Flood routing in two dimensions is handled through a numerical integration of the equations of motion and volume conservation within each cell in eight directions. The simple volume conservation governing equations are written as general constitutive fluid equations, which include the continuity equation and the dynamic wave momentum equation [8].

The 2D hydrodynamic model was used to develop a floodplain inundation model for a 120 km river reach at the outlet of Mara river basin (Figure 9). The main channel was represented by a one-dimensional linear channel based on fifty surveyed river cross-sections and the floodplain topography was represented by a calibrated digital terrain model based on Advanced Space borne Thermal Emission and Reflection Radiometer Global Digital Elevation Model version 2 (ASTERDEM). The ASTER DEM was pre-processed to remove noise by using 2D Kalman filtering techniques [66,67]. The floodplain model domain was discretized into 100 m by 100 m grid cells. The upstream model boundary was

represented as a daily time-flow boundary condition at Mara Mine (5H2) station (3) and at Tigithe Bridge (2) while the downstream boundary condition as the levels of Lake Victoria (6). An internal river gauge at point 5 was used for model performance assessment (Figure 1).

The model was calibrated by determining optimum floodplain n_p and channel n_c roughness parameters. The optimum floodplain plain roughness parameter was found by setting river channel roughness at 0.03 $m^{-1/3}/s$. The optimum value of river channel roughness was obtained from instream sediment characteristics using median sediment particle diameter in meter and applying strickler formula developed in 1923 [68] and then adjusted accordingly by factors proposed by Arcrement and Schneider [16]. After which the calibrated river channel roughness parameter was determined through sensitivity analysis by varying its parameters while maintaining floodplain roughness at optimized value and evaluating the model performance. The model performance was evaluated at the internal gauging station using daily water level records. Model performance was evaluated based on the fit between simulated and observed water levels, using the Root Mean Square Error (RMSE), the Nash-Sutcliffe model efficiency coefficient (E) and the index of agreement (d) [69,70]. Different parameterizations of surface roughness were evaluated by comparing model performance. The three water surface simulations from the hydraulic model were analyzed to find out if use of spartial hydraulic roughness improves the modeling results hence a better model. The model results analyzed to show model improvement included; (1) Optimum floodplain roughness (n_p) with channel roughness n_c = 0.03 $m^{-1/3}/s$; (2) calibrated floodplain roughness (n_p) and channel roughness n_c; and (3) calibrated channel roughness n_c and spatial Manning's coefficients as derived with aid of relative surface roughness. A six-month period was simulated from 30 January 2004 to 30 June 2012 including a major flood event to capture model behavior during floods.

4. Results

4.1. Riparian Vegetation Mapping

The vegetation mapping accuracy assessment results are shown in Table 4. The overall accuracy for the seven classes was 69% with a Kappa Coefficient of 0.624. The resulting land cover map of the study area is presented in Figure 9. Only a relatively low overall accuracy could be achieved, due to the mixed character of some vegetation classes (Table 4). Especially the papyrus, the most dominant vegetation type can be mixed with other types. At some areas of the floodplain, dense and thick papyrus is the dominant cover (Papyrus/thicket), mapped with a relatively high producers accuracy. In the upper reach, dense thicket and shrub areas could not be separated well from the papyrus and regenerated papyrus, due to their spectral signature resemblance and patchy distribution. In Figure 9, it can be seen that the dense papyrus vegetation is dominantly present near the main river channel. The class of partially submerged vegetation and papyrus has lower mapping accuracies due to its patchy distribution, especially in the upstream part of the wetland. Swampy areas are areas dominated by frequently flooded grasslands, so during the dry season these areas characterized by healthy grass, which could be mapped with the lowest accuracies among the natural wetland vegetation classes. Vegetation class 7 (agriculture/bare land) was virtually having the highest classification accuracy, but this is represented with a very small proportion in the wetland. Due to the above-described limitations, we accepted this result, since the classification

accuracy of all classes was above 60%. Some other methods, such as data fusion between optical and SAR imagery may have produced better results, since SAR can provide structural attributes of different vegetation patterns [71]. Understanding the limitations, these results were used in the roughness parameterization.

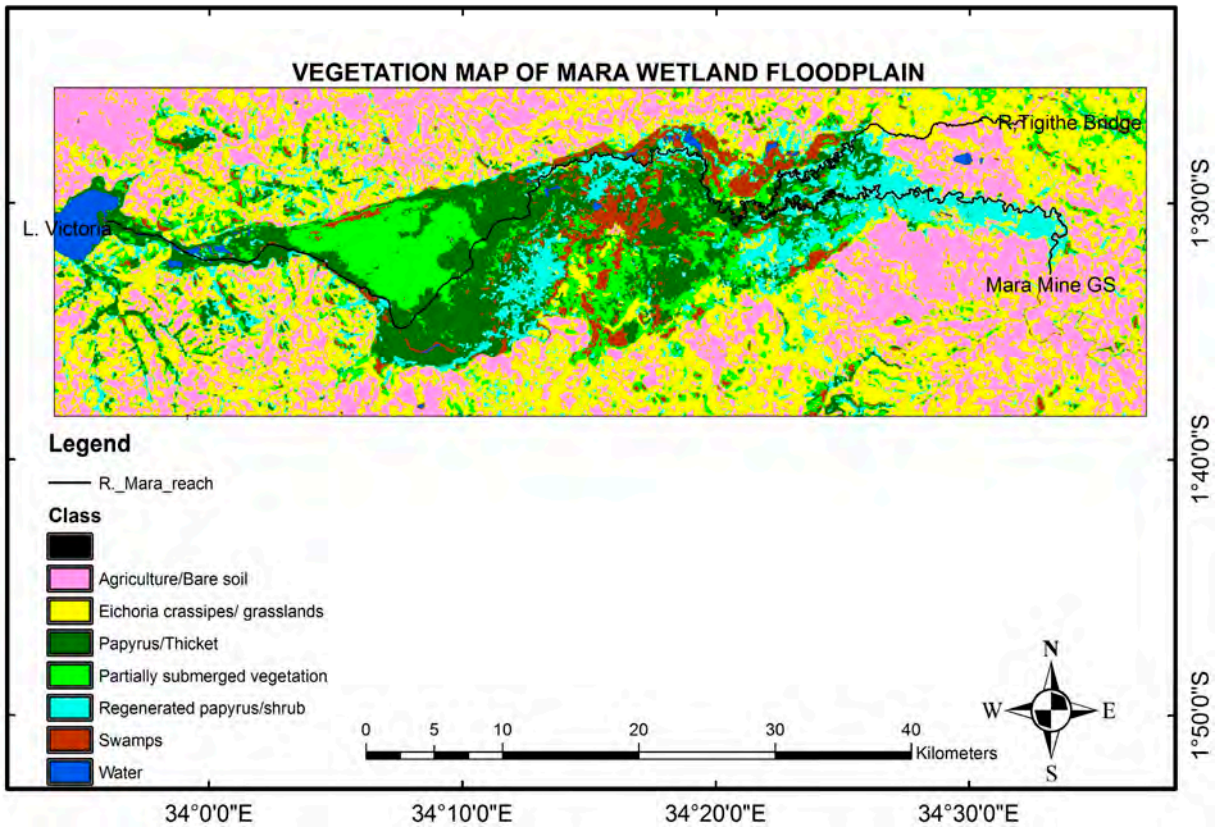

Figure 9. Vegetation map of Mara wetland floodplain showing seven classes of vegetation types.

Table 4. Supervised Classification Accuracy Assessments.

S/No	Class Name	Reference	Classified	Correct	Producers Accuracy (%)	User Accuracy (%)	Kappa
1	Water	11	9	6	54.6	66.67	0.654
2	Swamps	31	34	21	67.7	61.76	0.574
3	Partially submerged vegetation	61	58	38	62.0	65.52	0.567
4	Papyrus/thicket	75	78	54	72.0	69.23	0.589
5	Regenerated papyrus/shrub	56	52	37	66.0	71.15	0.645
6	Eichorhoea crassipes/Grassland	37	43	29	78.38	67.44	0.628
7	Agriculture/Bareland	29	26	22	75.86	84.62	0.829
	TOTAL	300	300	207	Average		0.624

Overall Classification Accuracy = 69.00%, Kappa Coefficient = 0.624.

4.1. Relative Surface Roughness

Relative surface roughness results shows that densely vegetated areas have higher values than less dense areas. For example densely vegetated papyrus vegetation and savannah grasslands have K_s of the

same order. These indicate that the K_s contains vegetation characteristics that can be used for spatial hydraulic roughness parameterization. Figure 10 below shows map of K_s at a scale of 0 to 1.

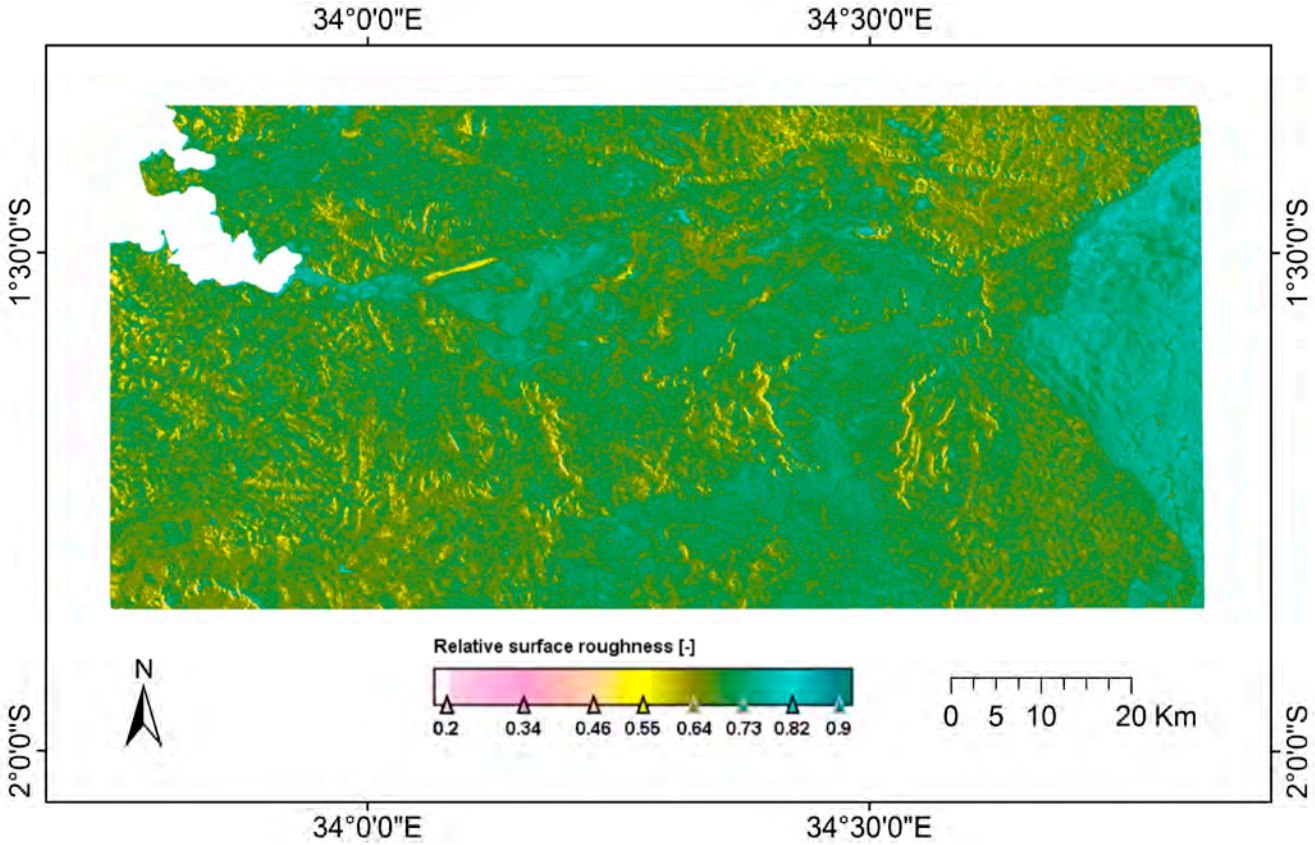

Figure 10. Relative surface roughness (K_s) of the study area on a scale of 0 to 1.

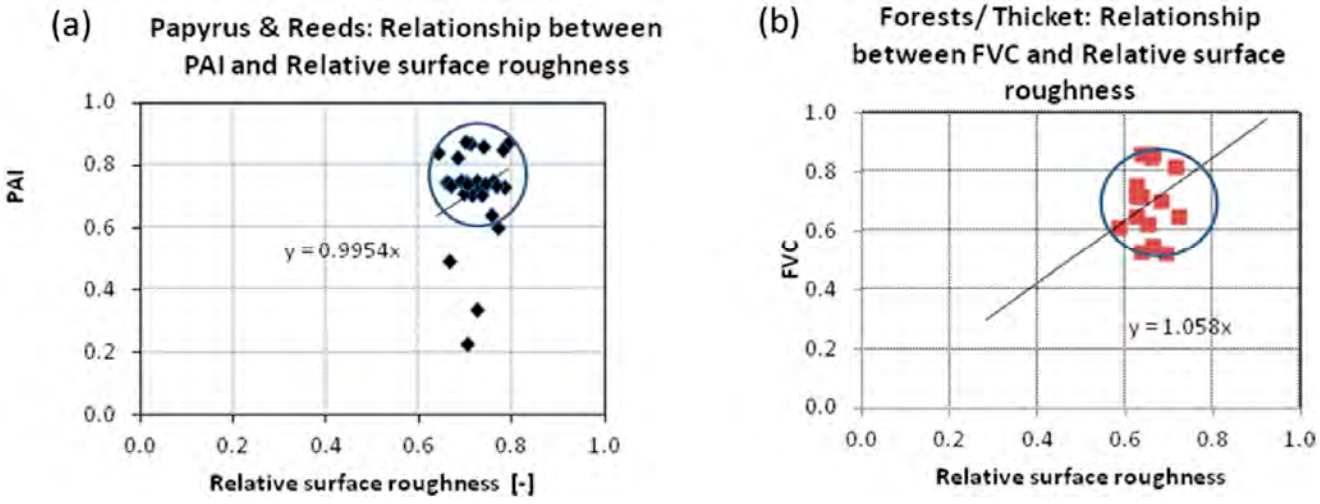

Figure 11. Correlation between Plant Area Index (PAI) and Fractional Vegetation Cover (FVC) against relative surface roughness. The correlation coefficient for plots (**a**), (**b**), are 0.03, 0.08, respectively.

Direct field verification of Manning's roughness values was practically not feasible. Nevertheless, the derived remote sensing based relative surface roughness was correlated to PAI and FVC to check if these vegetation attributes are reflected in the SAR relative surface roughness values. The relative

roughness and Manning's roughness were extracted at locations where PAI and FVC were determined on the site. These values were plotted to determine whether they are correlated (Figure 11). Within vegetation sampled, PAI or FVC *versus* relative roughness has an agreement in the shape but week positive linear correlation. These show that relative surface roughness may not be directly related to PAI or FVC (Figure 11a,b). It can support determination of vegetation attributes variations within the vegetation type that is directly related to spatial hydraulic roughness. From Figure 11 both vegetation types have relative surface roughness and Manning's roughness within a range of 0.6–0.8.These results does not prove beyond reasonable doubt that there exists a relationship between PAI or FVC and K_s from the few data points collected.

The plots show good agreement in data spread but low correlation. The correlation between PAI and FVC against relative surface roughness was obtained to be 0.03 and 0.08, respectively, so it is not possible to relate K_s to these parameters, which are easy to define in the field. The major limitation is that the backscatter is defined by the surface and the whole volume of the vegetation canopy, whilst the effective hydraulic roughness on the forested floodplains is defined by the lower part of the vegetation, since water levels are usually under the crown base height.

4.2. Roughness Map

There are overlaps of relative surface roughness ranges between land cover classes. The minimum relative roughness in this case is between 0.09 in swamps to 0.432 in water bodies (with waves), other classes fall within this range. The maximum relative surface roughness for all the classes lies between 0.89 for swamps and 0.92 for open water bodies. The standard deviation of relative surface roughness was observed to be below 0.06 for all classes except on swampy and grassland areas with standard deviation of the relative roughness values of 0.68 and 0.38, respectively. The average relative surface roughness values for all the seven classes were between 0.6 and 0.78. The lowest mean was recorded in swampy areas and highest mean in water bodies. Table 5 below shows minimum, average, maximum K_s and calculated average Manning's coefficient per vegetation class.

Table 5. Relative surface roughness and calculated average Manning's for different vegetation classes.

No	Vegetation Class	$(K_s)_{min,c}$ (-)	$(K_s)_{ave}$ (-)	$(K_s)_{max,c}$ (-)	Calculated Average Manning's Coefficient ($m^{-1/3}/s$)
1	Water	0.43	0.78	0.92	0.07
2	Swamps	0.09	0.68	0.89	0.27
3	Partially submerged vegetation	0.20	0.69	0.89	0.39
4	Papyrus/Thicket	0.18	0.71	0.92	0.62
5	Regenerated papyrus/Shrub	0.41	0.70	0.89	0.32
6	Eichorrhoea Crassipes/Grassland	0.20	0.69	0.91	0.27
7	Agriculture/bare soil	0.27	0.70	0.90	0.24

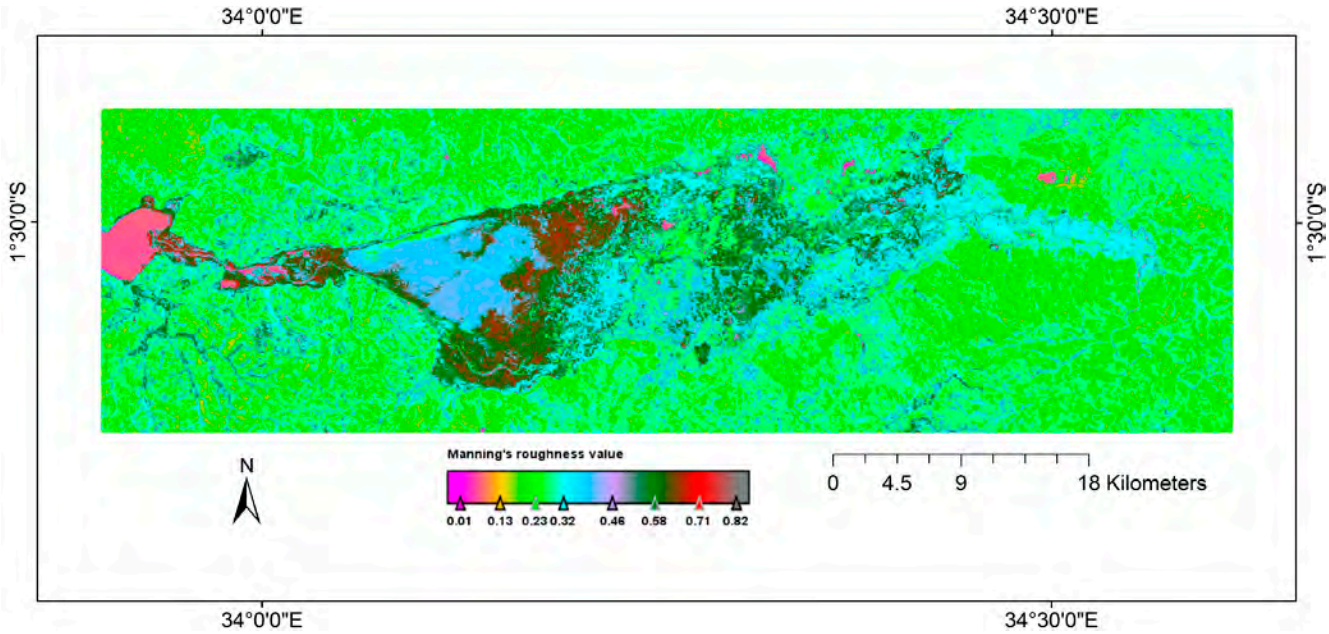

Figure 12. Spatial Manning's roughness coefficient ($m^{-1/3}/s$) derived from Landsat TM based vegetation map and relative surface roughness from SAR imagery.

The spatial roughness map was produced using Equation (4). The result in Figure 12 indicates that water bodies have low values while densely vegetated papyrus vegetation has higher values. This can give a qualitative indication that the approach used in determination of the spatial hydraulic roughness is appropriate.

4.2. Hydraulic Modeling Results

Calibration and sensitivity analysis of single Manning's roughness on model performance was evaluated based on Nash—Sutcliffe efficiency criterion (E) and Root mean square error (RMSE). The model was run for a range of single values of floodplain friction from between 0.2 $m^{-1/3}/s$ and 0.85 $m^{-1/3}/s$ at increment of 0.05 $m^{-1/3}/s$ (around 14 simulations in total). The results are shown in Table 6 and Figure 13 shows the model performance during the flood event from 21 April to 30 June 2012. The results indicate that at the internal gauging station 2, the single floodplain friction value for optimum performance is 0.65 $m^{-1//3}/s$, which yield 0.92 and 0.02 m for E and RSME, respectively.

Table 6. Model performance parameter as per different single friction roughness parameterizations.

Run No.	1	2	3	4	5	6	7	8	9	10	11	12	13	14
N ($m^{-1//3}/s$)	0.2	0.25	0.3	0.35	0.4	0.45	0.5	0.55	0.6	0.65	0.7	0.75	0.8	0.85
E	0.22	0.28	0.43	0.50	0.56	0.65	0.74	0.84	0.89	0.92	0.84	0.74	0.60	0.50
RMSE (m)	0.35	0.25	0.19	0.16	0.13	0.092	0.08	0.062	0.03	0.02	0.031	0.04	0.075	0.12

The modeling results due to hydraulic roughness parameterizations were evaluated based on the simulated hydrographs for (1) optimum floodplain roughness (n_p) with channel roughness n_c = 0.03 $m^{-1/3}/s$(SWL1); (2) calibrated values for both floodplain roughness(n_p) and channel roughness n_c (SWL2); and (3) calibrated channel roughness n_c and spatial Manning's coefficients as derived with

aid of relative surface roughness(SWL3). The emphasis was put in the capturing of flood events when the flows are spread in the floodplain. The results of three simulations for the six-month period of from 30 January 2004 to 30 June 2012 including a major flood event are shown Figure 14 below. A bank-full level at internal gauging station 5 is provided in the figure below for reference purposes of flood wave characterization above which flow extends to the floodplain. The results discussed include results from partially calibrated model (SWL1), Fully calibrated model (SWL2) and simulation using spatial Manning's coefficients as derived with aid of relative surface roughness (SWL3).

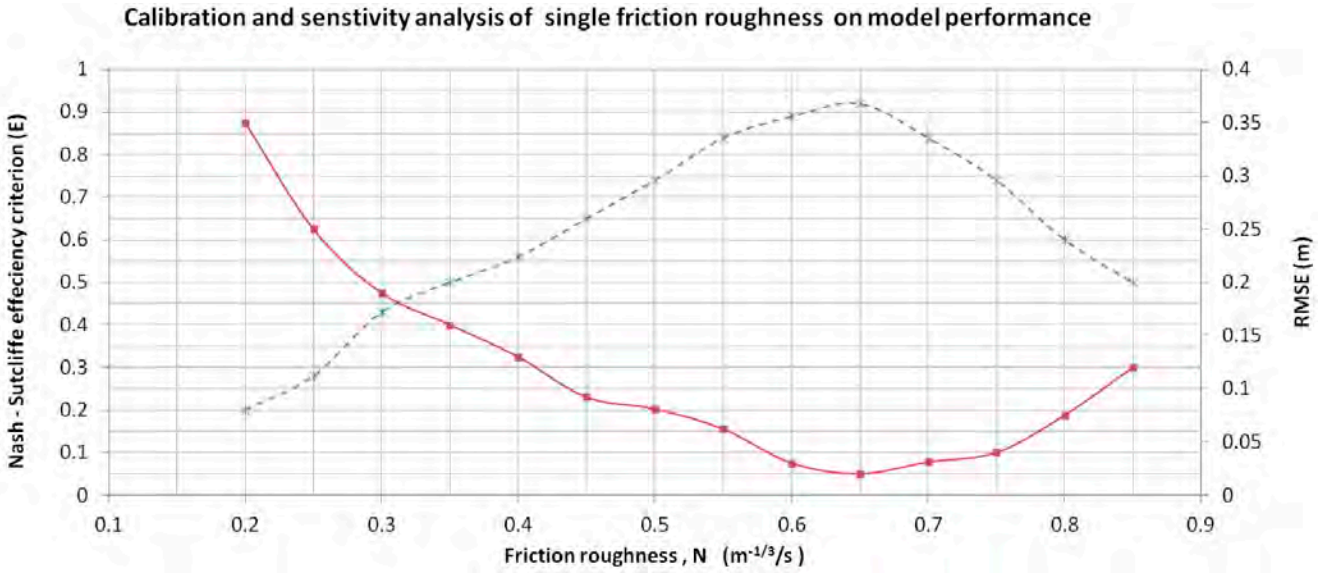

Figure 13. Calibration and sensitivity analysis of single friction roughness on model performance (SWL1). Friction roughness (*n*), Root Mean Square Error (RMSE) for observed and simulated water level hydrographs.

The resulting water stages are shown in Figure 14. OWL is the observed water level at the gauging station. SWL1 is simulated water levels with optimum floodplain roughness (n_p) with channel roughness n_c = 0.03 $m^{-1/3}$/s, SWL2 is simulated water levels with calibrated values for both floodplain roughness n_p = 0.65 $m^{-1/3}$/s and channel roughness n_c = 0.021 $m^{-1/3}$/s and SWL3 is simulated water levels with calibrated channel roughness n_c and spatial Manning's coefficients as derived with aid of relative surface roughness.

The model performance for the three simulations results is presented in Table. 7. The overall performance for scenario 3 for the whole simulated period is superior as it is proved by the better performance statistics of E = 0.97 compared to calibrated model E = 0.94. The use of spatial roughness parameterization improved the model performance in comparison to the calibrated model but also improved model performance significantly in capturing low flows stages. For this case it can be seen that spatial roughness parameterization can improve flood wave progression modeling without calibrating the Manning's roughness value for the whole floodplain. Scenarios 2 and 3 slightly overestimate the water levels, but the errors are higher in capturing the peaks in scenario 1. In scenario 2 and 3, water stages at low flows are overestimated this may be explained by uncertainty of accuracy of topographic data and downstream boundary condition. At high flood events the hydrographs are captured well at high flows for SWL1 and SWL2 simulations. During flood events or periods the calibrated model and

that parametrized using spartial roughness derived from relative roughness performed equally. The results in Figure 13 also indicate that the model is sensitive to river channel roughness parameter.

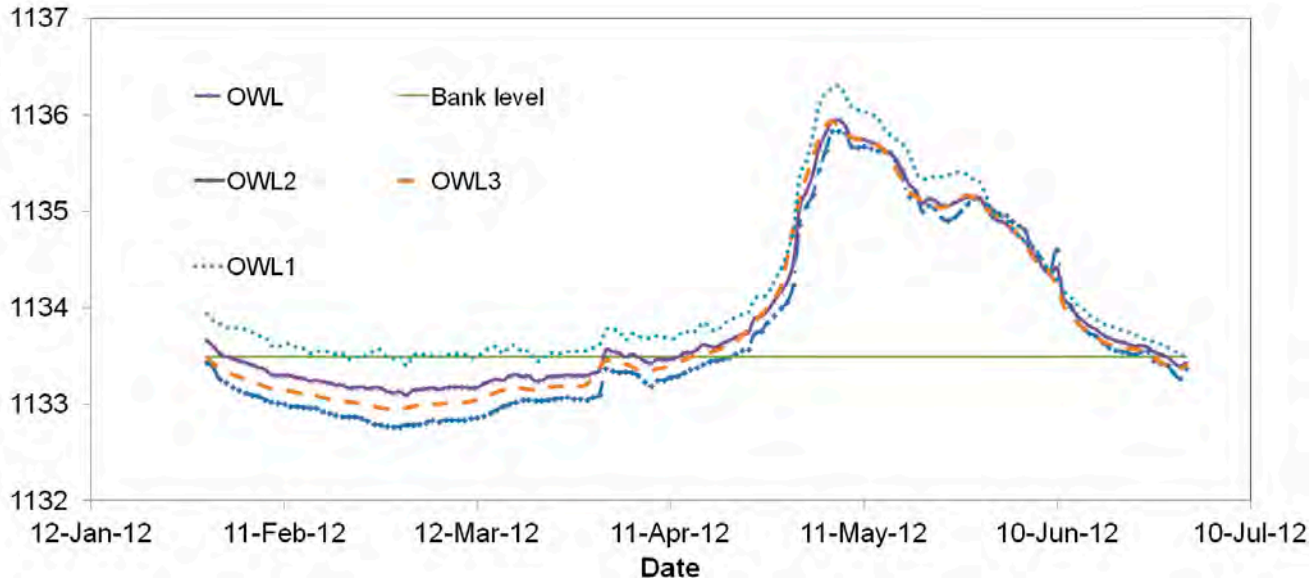

Figure 14. Observed and simulated hydrographs for three simulations SWL1, SWL2 and SWL3.

Table 7. Model performance parameter as per different Manning's roughness parameterizations. SWL1 is simulated water levels with optimum floodplain roughness (n_p) with channel roughness n_c = 0.03 $m^{-1/3}/s$, SWL2 is simulated water levels with calibrated values for both floodplain roughness (n_p) and channel roughness n_c and SWL3 is simulated water levels with calibrated channel roughness (n_c) and spatial Manning's coefficients as derived with aid of relative surface roughness The values outside the bracket represent the overall performance for the period of 21 April 2004 to 30 June 2012, whilst the ones in the brackets represent model evaluation during flood event from 21 April 2004 to 30 June 2012.

Performance Criteria	Scenario 1 (SWL1)	Scenario2 (SWL2)	Scenario 3 (SWL3)
Nash—Sutcliffe efficiency criterion (E)	0.75 (0.85)	0.95(0.98)	0.97 (0.96)
Index of agreement (d)	0.93 (0.97)	0.98(0.99)	0.99 (0.99)
Bias (%)	0.036 (0.022)	0.016(0.006)	0.009 (0.005)
STEYX (m)	0.185 (0.188)	0.085(0.086)	0.106 (0.149)
RMSE (m)	0.22 (0.05)	0.047(0.006)	0.023 (0.11)
Coefficient of Determination (R^2)	0.95 (0.95)	0.99(0.99)	0.98 (0.97)

During low flows all the simulated water levels are higher than the observed water levels. This may be due to the simplified parameterization of the river channel in the model among others. During flooding the water inundates the floodplain, where the parameterization of the resistance against flow in the vegetated riparian areas is becoming important in simulating the water levels.

5. Conclusions

The overall performance of scenario SWL1 is simulated water levels with optimum floodplain roughness (n_p = 0.65) with channel roughness n_c = 0.03 $m^{-1/3}/s$ was characterized with E = 0.75 and R^2 = 0.95, which was improved in SWL2 during full model calibration with calibrated values for both floodplain roughness n_p = 0.65 $m^{-1/3}/s$ and channel roughness n_c = 0.021 $m^{-1/3}/s$. In SWL2 simulations the model performance was observed to increase to E = 0.95 and R^2 = 0.99. When spatially distributed Manning values derived from SAR relative surface values were parametrized in the model, the model also performed well and yielding E = 0.97 and R^2 = 0.98. Improved model performance using spatial roughness shows that spatial roughness parameterization can support flood modeling and provide better flood wave simulation over the inundated riparian areas equally as calibrated models. Important water level differences were observed between the three roughness coefficient parameterizations. Nevertheless, there was no major difference in the timing of the flood peak. The calibration of Manning's roughness value (Figure 13) that optimum value for friction roughness is 0.65 $m^{-1//3}/s$ which model performance of E = 0.92 and RMSE = 0.02 m. Using spatial roughness for model parameterization also yielded values E = 0.85 and RMSE = 0.05 m. This shows that spatial parameterization of roughness using SAR properties may improve the model performance equally as calibrated model. These results are limited to the model setup characteristics that include grid size, river channel presentation, and stability criteria. Further sources of error can be found in the inherent inaccuracies in the satellite image processing steps. First of all, the unavoidable inaccuracies of the optical satellite image classification. This contributes to the observed overlaps between the relative roughness ranges of the different vegetation types. Speckle in SAR images was suppressed by a median filtering, but this cannot completely remove this noise, which results in an unknown level of inaccuracy in the calculated relative surface roughness values.

The reasons for the observed discrepancies may be as complex as the floodplain itself, which will need careful further research. First of all, the (in) accuracy of the topographical data and the model mesh resolution need to be investigated. In addition, topography interacts with spatially-distributed friction in a complex manner in the timings of the flood wave. In some studies, adaptive time-step of storage cell models have been shown to increase sensitivity to floodplain friction [72]. For the above results the model performance was good when calibrated and spatial roughness were implemented in the model. The added advantage of spatial parametrization is on the simulation time when calibration requires more simulations. The model needs further validation of the spatial distribution of the simulated inundation using satellite image based actual flood maps. The spatial inundation extent during peak flood event needs to be validated using satellite imagery. In addition, topography and spatially-distributed friction interacted with the flow in a complex manner, which could not be fully parameterized all over the floodplain, but our study made an important step in understanding and predicting flood inundation dynamics in riparian areas. Further research is still required to investigate if complex hydrodynamic models (e.g., DELFT 2D/3D, MIKE 21, SOBEK) utilizing full Saint Vennant's equations could perform better than FLO-2D in data scarce areas.

Usefulness of SAR for spatial hydraulic parameterization for hydraulic modeling has been shown in this paper. Temporal variation analysis of backscatter can support spatial hydraulic roughness parameterization of finite volume conservative hydrodynamic models. The use of spatially-distributed

friction (Manning's) coefficients as presented here in detail have not been shown in previous studies. Spatially distributed friction coefficients have important effects on hydrodynamic model performance affecting predicted flood depths. These results show that quantification of spatially distributed Manning's roughness can equally improves the performance of hydraulic models as calibrated model for large flood plains. These models are computationally expensive and cannot be automatically calibrated for large floodplains. As a summary, we can state that our study made a step in understanding and predicting flood inundation dynamics in riparian areas based on SAR images, those can provide information even under thick cloud cover. With the upcoming availability of new remote sensing data with higher revisiting frequencies, e.g., Senitel-1 with its SAR sensor and Sentinel-2 with its high-resolution optical data, a unique opportunity opens in monitoring riparian ecosystems for supporting flood modeling with more accurate data for the parameterization of hydraulic resistances.

Acknowledgments

This work was primarily supported by the European Space Agency (ESA) ALCANTARA project AO/1-7102/12- A15, which supported remote sensed data acquisition, field visit and one year fellowship opportunity to conduct this study at ITC, University of Twente, The Netherlands. The author would like to acknowledge the support of the Mara *flows* Project (UPaRF UNESCO-IHE) and the University of Dar es Salaam who initiated this study and provided PhD fellowship support to study at the University of Dar es Salaam. Special thanks to TIGER project No. 24, the RADARSAT-2 Science and Operational Applications Research and Development Program ("SOAR Program") No. 5126 of the Canadian Space Agency for their support in SAR data aquisation. Special thanks to FLO-2D Software *Inc*—Arizona, USA for hydrodynamic model used in this study. Thanks for Lake Victoria basin Office for providing the meteorological data and support during fieldwork. Authors express their special thanks to Jonathan Mwania for his help in field data collection.

Author Contributions

All authors contributed extensively to the work presented in this paper. Specific contributions include development of the modeling concept and use of SAR data, provision of data and data acquisition capacity (Preksedis Ndomba, Felix Mtalo, Zoltan Vekerdy); fieldwork, model development, data pre-processing, analysis and preparation manuscript and figures (Joseph Mtamba, Rogier van der Velde, Preksedis Ndomba, Zoltan Vekerdy). Final proof reading of the manuscript was done by Rogier van der Velde, Zoltan Vekerdy, and Felix Mtalo).

Conflicts of Interest

The authors declare no conflict of interest.

References

1. Junk W.; Barley P.B.; Sparks R.E. The flood pulse concept in river flood plain systems. *Can. J. Fish. Aquat. Sci.* **1989**, *106*, 110–127.

2. Poff, N.L.; Allan, J.D.; Bain, M.B.; Karr, J.R.; Prestegaard, K.L.; Richter, B.; Sparks, R.; Stromberget, J. The natural flow regime: A new paradigm for riverine conservation and restoration. *BioScience* **1997**, *47*, 769–784.
3. Postel, S.L.; Richter, B. *Rivers for Life: Managing Water for People and Nature*; Island Press: Washington, DC, USA, 2003.
4. Bunn S.E.; Arthington A.H. Basic principles and ecological consequences of altered flow regimes for aquatic biodiversity. *Environ. Manag.* **2002**, *30*, 492–507.
5. Casas, A.; Lane, S.N.; Yu, D.; Benito, G. A method of parameterising roughness and topographic sub-grid scale effects in hydraulic modelling from LiDAR data. *Hydrol. Earth Syst. Sci.* **2010**, *14*, 1567–1579.
6. Bates, P.; Anderson, M.G.; Walling, D.E.; Simm, D. Modelling floodplain flows using a two-dimensional finite element model. *Earth Surf. Proc. Land* **1992**, *17*, 575–588.
7. Stoesser, T.; Wilson, C.A.M.E.; Bates, P.; Dittrich, A. Application of a 3D numerical model to a river with vegetated floodplains. *J. Hydroinf.* **2003**, *5*, 99–112.
8. O'Brien, J.S. *FLO-2D Reference Manual*; FLO-2D Inc.: Nutrioso, AZ, USA, 2009.
9. Bates, P.D.; de Roo, A.P.J. A simple raster-based model for flood inundation simulation. *J. Hydrol.* **2000**, *236*, 54–77.
10. Horritt M.S.; Bates P.D. Evaluation of 1D and 2D numerical models for predicting river flood inundation. *J. Hydrol.* **2002**, *268*, 87–99.
11. Forzieri, G.; Degetto, M.; Righetti,M.; Castelli, F.; Preti, F. Satellite multispectral data for improved floodplain roughness modelling. *J. Hydrol.* **2011**, *407*, 41–57.
12. Tarekegn, T.H.; Haile, A.H.; Rientjes, T.; Reggiani, P.; Alkema, D. Assessment of an ASTER-generated DEM for 2D hydrodynamic flood modelling. *Int. J. Appl. Earth Observ. Geoinf.* **2010**, *12*, 457–465.
13. Rutherfurd, I.D.; Hoang, T.; Prosser, I.P; Abernethy, B.; Jayasuriya, N. The impact of gully networks on the time-to-peak and size of flood hydrographs. In Proceedings of 23rd Hydrology and Water Resources Symposium, Hobart, TAS, Australia, 21–24 May 1996; Institution of Engineers, Australia NCP 96-05: Canberra, NSW, Australia, 1996; pp. 397–402.
14. Anderson, B.G.; Rutherfurd, I.D.; Western, A.W. An analysis of the influence of riparian vegetation on the propagation of flood waves. *Environ. Model. Softw.* **2006**, *21*, 1290–1296.
15. Chow, V.T. *Open Channel Hydraulics*; McGraw-Hill: New York, NY, USA, 1959.
16. Arcement, G.J. Jr.; Schneider, V.R. *Guide for Selecting Manning's Roughness Coefficients for Natural Channels and Flood Plains*; Water-Supply Paper 2339; US Geological Survey: Washington, DC, USA, 1989.
17. Baptist, M.J.; van den Bosch, L.V.; Dijkstra, J.T.; Kapinga, S. Modelling the effects of vegetation on flow and morphology in rivers. *Large Rivers* **2005**, *15*, 339–357.
18. Straatsma, M.W.; Middelkoop, H. Extracting structural characteristics of herbaceous floodplain vegetation under leaf-off conditions using airborne laser scanner data. *Int. J. Remote Sens.* **2007**, *28*, 2447–2467.
19. Dudley, S.J.; Bonham, C.D.; Abt, S.R.; Fischenich, J.G. Comparison of methods for measuring woody riparian vegetation density. *J. Arid Environ.* **1998**, *38*, 77–86.

20. Forzieri, G.; Guarnieri, L.; Vivoni, E.R.; Castelli, F.; Preti, F. Spectral-ALS data fusion for different roughness parameterizations of forested floodplains. *River Res. Appl.* **2010**, *27*, 826–840.
21. Forzieri, G.; Moser, G.; Vivoni, E.R.; Castelli, F. Riparian vegetation mapping for hydraulic roughness estimation using very high resolution remote sensing and LiDAR data fusion. *J. Hydraul. Eng.* **2010**, *11*, 855–867.
22. Mathieu, R.; Naidoo, L.; Cho, M.A.; Leblon, B.; Main, R.; Wessels, K; Asner, G.P; Buckley, J.; Aardt, J.V.; Erasmus, B.F.N.; *et al.* Toward structural assessment of semi-arid African savannahs and woodlands: The potential of multitemporal polarimetric RADARSAT-2 fine beam images. *Remote Sens. Environ.* **2013**, *138*, 215–231.
23. Straatsma, M.W.; Baptist, M.J. Floodplain roughness parameterization using airborne laser scanning and spectral remote sensing. *Remote Sens. Environ.* **2008**, *112*, 1062–1080.
24. Forzieri, G.; Castelli, F.; Preti, F. Advances in remote sensing of hydraulic roughness. *Int. J. Remote Sens.* **2011**, *33*, 630–654.
25. Nagler, P.L.; Glenn, E.P.; Huete, A.R. Assessment of spectral vegetation indices for riparian vegetation in the Colorado River Delta, Mexico. *J. Arid Environ.* **2001**, *49*, 91–110.
26. Townsend, P.A.; Walsh, J. Remote sensing of forested wetlands: Application of multitemporal and multispectral satellite imagery to determine plant community composition and structure in southeastern USA. *Plant Ecol.* **2001**, *157*, 129–149.
27. Congalton, R.G.; Birch, K.; Jones, R.; Schriever, J. Evaluating remotely sensed techniques for mapping riparian vegetation. *Comput. Electron. Agric.* **2002**, *37*, 113–126.
28. Wilson, M.D.; Atkinson, P.M. The use of remotely sense data to derive floodplain friction coefficients for flood inundation modelling. *Hydrolog. Process.* **2007**, *21*, 3576–3586.
29. Makkeasorn, A.; Chang, N.-B.; Li, J. Seasonal change detection of riparian zones with remote sensing images and genetic programming in a semi-arid watershed. *J. Environ. Manag.* **2009**, *902*, 1069–1080.
30. Akasheh, O.Z.; Neale, C.M.U.; Jayanthi, H. Detailed mapping of riparian vegetation in the middle Rio Grande River using high resolution multi-spectral airborne remote sensing. *J. Arid Environ.* **2008**, *72*, 1734–1744.
31. Mason, D.; Cobby, D.M.; Horritt, M.; Bates, P. Floodplain friction parameterization in two-dimensional river flood models using vegetation heights from airborne scanning laser altimetry. *Hydrol. Processes* **2003**, *17*, 1711–1732.
32. Van der Velde, R.; Su, Z.; Ma, Y. Impact of soil moisture dynamics on ASAR σ° signatures and its spatial variability observed over the Tibetan Plateau. *Sensors* **2008**, *8*, 5479–5491.
33. Van der Velde, R.; Su, Z.; van Oevelen, P.; Wen, J.; Ma, Y.; Salama, M.S. Soil moisture mapping over the central part of the Tibetan Plateau using a series of ASAR WS images. *Remote Sens. Environ.* **2012**, *120*, 175–187.
34. Kuenzer, C.; Guo, H.; Huth, J.; Leinenkugel, P.; Li, X.; Dech, S. Flood mapping and flood dynamics of the Mekong Delta: ENVISAT-ASAR-WSM based time series analyses. *Remote Sens.* **2013**, *5*, 687–715.
35. Schumann, G.; di Baldassarre, G.; Bates P.D. The utility of space-borne radar to render flood inundation maps based on multi-algorithm ensembles. *IEEE Trans. Geosci. Remote Sens.* **2009**, *47*, 2801–2807.

36. Schumann, G.J.-P.; Bates P.D.; Horritt, M.S.; Matgen, P.; Pappenberger, F. Progress in integration of remote sensing derived flood extent and stage data and hydraulic models. *Rev. Geophys.* **2009**, doi:10.1029/2008RG000274.
37. Ferrazzoli, P.; Paloscia, S.; Pampaloni, P.; Schiavon, G.; Sigismondi, S.; Solamini, D. The potential of multifrequency polarimetric SAR in assessing agriculture and arboreous biomass. *IEEE Trans. Geosci. Remote Sens.* **1997**, *35*, 5–15.
38. Alberga, V.; Satalino, G.; Staykova, D.K. Comparison of polarimetric SAR observables in terms of classification performance. *Int. J. Remote Sens.* **2008**, *29*, 4129–4150.
39. Cloude, R.S.; Pottier, E. An entrophy based classification scheme for land applications of polarimetric SAR. *IEEE Trans. Geosci. Remote Sens.* **1997**, *35*, 68–78.
40. Lucas, R.M.; Cronin, N.; Lee, A.; Moghaddam, M.; Witte, C.; Tickle, P. Empirical relationships between AIRSAR backscatter and LiDAR-derived forest biomass, Queensland, Australia. *Remote Sens. Environ.* **2006**, *100*, 407–425.
41. Englhart, S.; Keuck, V.; Siegert, F. Aboveground biomass retrieval in tropical forests—The potential of combined X- and L-band SAR data use. *Remote Sens. Environ.* **2011**, *115*, 1260–1271.
42. Garestier, F.; Dubois-Fernandez, P.C.; Guyon, D.; le Toan, T. Forest biophysical parameter estimation using L- and P-band polarimetric SAR data. *IEEE Trans. Geosci. Remote Sens.* **2009**, *47*, 3379–3388.
43. Lewis, A.J.; Henderson, F.M. Radar fundamentals: The geoscience perspective. In *Principles and Applications of Imaging Radar: Manual of Remote Sensing*, Third ed.; Henderson, F.M., Lewis, A.J., Eds.; John Wiley & Sons: New York, NY, USA, 1998; Volume 2, pp. 131–181.
44. Verhoest, N.E.; Lievens, H.; Wagner, W.; Álvarez-Mozos, J.; Moran, M.S.; Mattia, F. On the soil roughness parameterization problem in soil moisture retrieval of bare surfaces from synthetic aperture radar. *Sensors* **2008**, *8*, 4213–4248.
45. Ranson K.J.; Sun, G. Mapping biomass of a northern forest using multifrequency SAR data. *IEEE Trans. Geosci. Remote Sens.* **1994**, *32*, 388–396.
46. Mattia, F.; Toan, L.T.; Souyris, J.-C.; Carolis, G.D.; Floury, N.; Posa, F. The effect of surface roughness on multifrequency polarimetric SAR data. *IEEE Trans. Geosci. Remote Sens.* **1997**, *35*, 954–966.
47. Mtamba, J.O.D.; Ndomba, P.M.; Mtalo, F.; Crosato, A. Hydraulic study of flood rating curve development in the Lower Mara Basin. In Proceedings of 4th International Multidisciplinary Conference on Hydrology and Ecology (HydroEco 2013), Rennes, France, 13–16 May 2013.
48. McClain, M.; Subalusky, A.; Anderson, E.; Dessu, S.; Melesse, A.; Ndomba, P.; Mtamba, J.; Tamatamah, R.; Mligo, C. Comparing flow regime, channel hydraulics and biological communities to infer flow-ecology relationships in the Mara River of Kenya and Tanzania. *Hydrol. Sci. J.* **2013**, doi:10.1080/02626667.2013.853121.
49. Breda, N.J.J. Ground-based measurements of leaf area index: A review of methods, instruments and current controversies. *J. Exp. Bot.* **2003**, *54*, 2403–2417.
50. Jonckheere, I.; Fleck, S.; Nackaerts, K.; Muys, B.; Coppin, P.; Weiss, M.; Baret, F. Review of methods for *in situ* leaf area index determination. Part I. Theories, sensors and hemispherical photography. *Agric. For. Meteorol.* **2004**, *121*, 19–35.

51. Weiss, M.; Baret, F.; Smith, G.J.; Jonckheere, I.; Coppin, P. Review of methods for *in situ* leaf area index (LAI) determination Part II. Estimation of LAI, errors and sampling. *Agric. For. Meteorol.* **2004**, *121*, 37–53.
52. Garrigues, S.; Shabanov, N.V.; Swanson, K.; Morisette, J.T.; Baret, F.; Myneni, R.B. Intercomparison and sensitivity analysis of leaf area index retrievals from LAI-2000, AccuPAR, and digital hemispherical photography over croplands. *Agric. For. Meteorol.* **2008**, *148*, 1193–1209.
53. Congalton, R.; Green, K. *Assessing the Accuracy of Remotely Sensed Data: Principles and Practices*, 2nd ed.; Lewis Publishers: Boca Raton, FL, USA, 1999.
54. Maghsoudi, Y.; Collins, M.J.; Leckie, D.G. On the use of feature selection for classifying multitemporal Radarsat-1 images for forest mapping. *IEEE Geosci. Remote Sens. Lett.* **2011**, *8*, 904–908.
55. Bruzzone, L.; Marconcini, M.; Wegmüller, M.; Wiesmann, A. An advanced system for the automatic classification of multitemporal SAR images. *IEEE Trans. Geosci. Remote Sens.* **2004**, *42*, 1321–1334.
56. Petryk, S.; Bosmajian, G.B. Analysis of flow through vegetation. *J. Hydraul. Div.* **1975**, *101*, 871–884.
57. Ogilvy, J.A.; Foster, J.R. Rough surfaces: Gausian or exponential statistics. *Phys. Rev. D Appl. Phys.* **1989**, *22*, 1243–1251.
58. Geman, S.; Geman, D. Stochastic relaxation, Gibbs distributions, and the Bayesian restoration of images. *IEEE Trans. Pattern Anal. Mach. Intell.* **1984**, *6*, 721–741.
59. Jeng, F; Woods, J. Compound Gauss-Markov random fields for image estimation. *IEEE Trans. Signal Process.* **1991**, *39*, 683–697.
60. Zhu, S.C.; Wu, Y.; Mumford, D. Filters, random fields and maximum entropy (FRAME): Towards a unified theory for texture modelling. *Int. J. Comput. Vis.* **1998**, *27*, 107–126.
61. Freeman, A.; Durden, S. A three-component scattering model for polarimetric SAR data. *IEEE Trans. Geosci. Remote Sens.* **1998**, *36*, 963–973.
62. Winkler, G. *Image Analysis, Random Fields and Markov Chain Monte Carlo Methods: A Mathematical Introduction*, 2nd ed.; Springer-Verlag Berlin Heidelberg: New York, NY, USA, 2003.
63. Kasetkasem, T.; Rakwatin, P.; Sirisommai, R.; Eiumnoh, A. A joint land cover mapping and image registration algorithm based on a markov random field model. *Remote Sens.* **2013**, *5*, 5089–5121.
64. Löw, A. Coupled Modelling Of Land Surface Microwave Interactions Using ENVISAT ASAR Data. Ph.D. Thesis, Ludwig Maximilian University of Munich, Munich, Germany, 2004.
65. Bates, P.D. Remote sensing and flood inundation modelling. *Hydrol. Proc.* **2004**, *18*, 2593–2597.
66. Wang, P. Applying two dimension kalman filtering for digital terrain modeling. In IAPRS, Proceedings of ISPRS Commission IV Symposium, GIS Between Visions and Applications, Stuttgart, Germany, 7–10 September 1998; Fritsch, D., Englich, M., Sester, M., Eds.; 32, pp.649–656. Available online: http://www.isprs.org/proceedings/XXXII/part4/wang71.pdf (Accessed on 20 March 2013).
67. Gallant, J.C.; Hutchinson, M.F. Producing Digital Elevation Models with Uncertainty Estimates Using a Multi-scale Kalman Filter. Available online: http://www.spatial-accuracy.org/book/export/html/183 (accessed on 14 May 2013).

68. Krause, P.; Boyle, D.P.; Base, F. Comparision of different efficiency criteria for hydrological model assessment. *Adv. Geosci.* **2005**, *5*, 89–97.
69. Hassanzadeh, Y. Hydraulics of Sediment Transport, Hydrodynamics—Theory and Model. Available online: http://www.intechopen.com/books/hydrodynamics-theory-and-model/hydraulics-of-sediment-transport (accessed on 25 December 2014).
70. Legates, D.R.; McCabe, G.J., Jr. Evaluating the use of "goodness-of-fit" measures in hydrologic and hydroclimatic model validation. *Water Resour. Res.* **1999**, *35*, 233–241.
71. Corcoran, J.; Knight, J.; Brisco, B.; Kaya, S.; Cull, A.; Murnaghan, K. The integration of optical, topographic, and radar data for wetland mapping in northern Minnesota. *Can. J. Remote Sens.* **2011**, *37*, 564–582.
72. Hunter, N.M.; Bates, P.D.; Horritt, M,S.; Wilson, M.D. Simple spatially-distributed models for predicting flood inundation: A review. *Geomorphology* **2007**, *90*, 208–225.